Point-spread function errors for weak lensing - density cross-correlations

Ziwen Zhang, Martin Kilbinger, Fabian Hervas Peters, Qinxun Li, Wentao Luo, Lucie Baumont, Jean-Charles Cuillandre, Sebastien Fabbro, Stephen Gwyn, Alan Mcconnachie, et al.

A&A, 691, A75 (2024)
https://doi.org/10.1051/0004-6361/202450623

Astronomy & Astrophysics

Point spread function errors for weak lensing – density cross-correlations

Application to UNIONS

Ziwen Zhang[1,2,3,⋆], Martin Kilbinger[1,⋆], Fabian Hervas Peters[1], Qinxun Li[4], Wentao Luo[2,3], Lucie Baumont[1], Jean-Charles Cuillandre[1], Sébastien Fabbro[5], Stephen Gwyn[5], Alan McConnachie[5], and Anna Wittje[6]

[1] Université Paris-Saclay, Université Paris Cité, CEA, CNRS, AIM, 91191 Gif-sur-Yvette, France
[2] CAS Key Laboratory for Research in Galaxies and Cosmology, Department of Astronomy, University of Science and Technology of China, Hefei, Anhui 230026, China
[3] School of Astronomy and Space Science, University of Science and Technology of China, Hefei 230026, China
[4] Department of Physics and Astronomy, University of Utah, Salt Lake City, Utah 84102, USA
[5] NRC Herzberg Astronomy & Astrophysics, 5071 West Saanich Road, British Columbia, V9E2E7 Canada
[6] Ruhr University Bochum, Faculty of Physics and Astronomy, Astronomical Institute (AIRUB), German Centre for Cosmological Lensing, 44780 Bochum, Germany

Received 6 May 2024 / Accepted 1 September 2024

ABSTRACT

Aims. Calibrating the point spread function (PSF) is a fundamental part of weak gravitational lensing analyses. Even with corrected galaxy images, imperfect calibrations can introduce biases. We propose an analytical framework for quantifying PSF-induced systematics as diagnostics for cross-correlation measurements of weak lensing with density tracers; for example, galaxy-galaxy lensing. We show how those systematics propagate to physical parameters of the density tracers. Those diagnostics only require a shape catalog of PSF stars and foreground galaxy positions.

Methods. We considered the PSF-induced multiplicative bias, and introduced three second-order statistics as additive biases. We computed both biases for the weak-lensing derived halo mass of spectroscopic foreground galaxy samples; in particular, their effect on the tangential shear and fit halo mass as a function of stellar mass. In addition, we assessed their impact on the recently published black-hole – halo-mass relation for type I active galactic nuclei (AGNs).

Results. Using weak-lensing catalogs from the Ultraviolet Near Infrared Optical Northern Survey (UNIONS) and the Dark Energy Survey (DES), we find the multiplicative biases in the tangential shear to be less than 0.5%. No correlations between additive bias and galaxy properties of the foreground sample are detected. The combined PSF systematics affect low-mass galaxies and small angular scales; halo mass estimates can be biased by up to 18% for a sample of central galaxies in the stellar mass range of $9.0 \leq \log M_*/\mathrm{M}_\odot < 9.5$.

Conclusions. The PSF-induced multiplicative bias is a subdominant contribution to current studies of weak-lensing – density cross-correlations, but might become significant for upcoming stage IV surveys. For samples with a low tangential shear, additive PSF systematics can induce a significant bias on derived properties such as the halo mass.

Key words. methods: statistical – galaxies: halos – cosmology: observations – large-scale structure of Universe

1. Introduction

Light from distant galaxies on its way to the observer is affected by gravitational fields along the line of sight, distorting the light distribution of the galaxies we observe. Weak gravitational lensing refers to the typical few-percent distortions of the galaxy image due to large-scale structure in the foreground (Jarvis et al. 2016). Weak lensing enables us to measure the distribution of the total foreground mass, which consists of baryonic and dark matter. Therefore, it is a powerful tool for studying cosmology (Kilbinger 2015; Mandelbaum 2018).

Among the main applications of weak lensing is galaxy-galaxy lensing, which is the correlation between the shapes of background galaxies and the positions of foreground galaxies. Many studies have used this method to estimate the (dark matter) halo mass, establishing various relations between the halo mass and galaxy properties (Mandelbaum et al. 2006; Leauthaud et al. 2012; Velander et al. 2014; Viola et al. 2015; Luo et al. 2018; Zhang et al. 2021, 2022, 2024).

There are a number of potential systematics that can bias weak-lensing measurements (Jarvis et al. 2016), such as: contamination from cosmic rays and satellite trails, charge-coupled device (CCD) effects including charge-transfer inefficiency, nonlinearity, or the brighter-fatter effect, which hinders the measurement of the galaxy brightness distribution; observed galaxy intensity profiles that may be contaminated by the flux from nearby galaxies or stars; and observed images of galaxies that are blurred due to atmospheric refraction or turbulence and optical imperfections. The combined effect of image blurring due to the atmosphere and the optical system is known as the point spread function (PSF; see for a recent focused review Liaudat et al. 2023).

The PSF can strongly smear the weak-lensing shear information in the observed galaxy shapes (Jarvis et al. 2021). In addition, the PSF is difficult to estimate because it varies with the field of view (FoV) and across individual exposures in

⋆ Corresponding author; martin.kilbinger@cea.fr, ziwen@mail.ustc.edu.cn

multi-epoch observations. Therefore, a central part of weak-lensing analyses and a formidable challenge is to correct for the PSF in observed galaxy images. Nevertheless, even after PSF correction, systematic errors can remain, induced by imperfections in the PSF model and the interpolation process (Jarvis et al. 2016).

Various methods exist to quantify PSF-induced systematics for weak lensing. For cosmic shear, the ρ statistics (Rowe 2010; Jarvis et al. 2016) are additive biases to the shear two-point correlation function and directly propagate to cosmological parameters. A generalisation is so-called τ statistics (Gatti et al. 2021) that allows one to separately estimate the impact of PSF leakage and PSF model errors on galaxy shapes. The PSF leakage quantifies, via the multiplicative parameter α, how much the PSF ellipticity influences the PSF-corrected galaxy ellipticity.

For galaxy-galaxy lensing, two kinds of null-test estimators have been developed. The first is the tangential shear around positions that are not correlated with the density tracers in an ideal setting. These can be random positions (Mandelbaum et al. 2005), stars, or points fixed to a CCD-frame coordinate system (Gatti et al. 2021). The second type of null test is the cross-component shear measured around the foreground sample, which is expected to vanish if parity is conserved.

So far, to the best of our knowledge, no PSF systematic diagnostics have been devised for lensing around foreground density tracers that directly propagate to parameters of the foreground population. Here, we have developed a set of three galaxy-PSF cross-correlation functions, which we dub "λ statistics", which are additive terms to the tangential shear around arbitrary density tracers such as galaxies, galaxy clusters, filaments, or voids. The λ statistics for weak lensing of density tracers are the analog of the ρ statistics for cosmic shear.

In the study of galaxy evolution, a common approach is to relate galaxy properties to their halo mass (scaling relation), and thus reveal the evolutionary paths of different galaxies in their dark matter environment (Posti et al. 2019; Zhang et al. 2021, 2022, 2024). We have examined two scaling relations in this paper; namely, the stellar-mass – halo-mass relation (SHMR) and the black-hole-mass – halo-mass relation. Various studies have investigated these relations in terms of analytic models (Bower et al. 2017), abundance matching (Shankar et al. 2020; Moster et al. 2010; Yang et al. 2009), and weak lensing (Zhang et al. 2024; Li et al. 2024). Of these, weak lensing is the most direct observational method for probing halo mass. The accuracy of scaling relations is affected by the accuracy of the halo mass estimates. In this paper, we have developed a method of quantifying the impact of PSF-induced systematics on the weak-lensing signal and also the halo mass estimates.

The outline of this paper is as follows. We describe the weak-lensing catalogs and the foreground sample selections in Sect. 2. Section 3 introduces the λ statistics, and presents the methods of quantifying PSF-induced multiplicative and additive biases for the weak-lensing tangential shear. This section also briefly reviews the measurement of tangential shear, and the connection of shear to halo mass. In Sect. 4, we show the results for PSF-induced multiplicative and additive biases. In addition, we investigate the impact of PSF-induced systematics on halo mass estimation. We discuss the implications of the λ statistics in Sect. 5 and summarize our results in Sect. 6. Throughout this paper, we assume the Planck cosmology (Planck Collaboration XIII 2016): $\Omega_{\rm m} = 0.307$, $\Omega_{\rm b} = 0.048$, $\Omega_\Lambda = 0.693$, and $h = 0.678$.

2. Observational data

2.1. Weak-lensing catalogs

2.1.1. UNIONS

We have used the weak-lensing shear catalog from the Ultraviolet Near-Infrared Northern Sky Survey (UNIONS). Started in 2018, UNIONS is an ongoing survey that targets 4800 deg^2 in the Northern Hemisphere and covers the footprint of the Euclid survey (Euclid Collaboration 2022). UNIONS combines multiband photometric images from different telescopes. These are the Canada-France Hawai'i Telescope (CFHT) providing u- and r-band images (this part of UNIONS is called the Canada-France Imaging Survey or CFIS); the Panoramic Survey Telescope and Rapid Response System (Pan-STARRS) for the i and z bands; Subaru, which takes images in the z band in the framework of WISHES (Wide Imaging with Subaru HSC of the Euclid Sky); and the g-band Waterloo Hawai'i IfA Survey (WHIGS). Here, we only use the UNIONS r-band data to calculate the weak-lensing shear. Shape measurement was performed with SHAPEPIPE (Farrens et al. 2022). A first version of the ShapePipe catalog was presented in Guinot et al. (2022). In this paper, we use v1.3 of the catalog, which contains 83, 812, 739 galaxies covering 3200 deg^2 of the effective sky area, which was the available data in 2022 at the time of processing. The PSF was modeled with MCCD (Liaudat et al. 2021), which builds a non-parametric multi-CCD model of the PSF over the focal plane. To obtain the parameters of the PSF model, we use the individual exposures to select stars. The star sample is defined by the stellar locus in the size – magnitude diagram. The stars were split into a training sample (80%) and a validation sample (20%). The PSF model was obtained by optimization using the training sample.

2.1.2. Dark Energy Survey

We also used the Dark Energy Survey (DES) Y3 weak-lensing catalog in our analysis (Gatti et al. 2021). The catalog contains 100, 204, 026 galaxies, covering 4139 deg^2 on the sky. Images were taken in the g, r, i, z, and Y bands and have a weighted source number density of 5.59 arcmin^{-2}. The corresponding shape noise is 0.261.

The DES star catalog contains 56 million objects, which were identified as stars using the stellar locus in the magnitude range [16.5, 22.0]. The PSF was modeled and interpolated using the PIFF algorithm (PSFs In the Full FOV, Jarvis et al. 2021). The parametric model for a star i was fit iteratively using neighbouring stars, rejecting outliers until convergence was reached. Each of the riz bands was fit separately. PIFF is intended to support fitting to the entire focal plane; however, the DES Y3 catalog is restricted to single CCD modeling.

2.2. Foreground galaxy catalogs

The following subsections describe the two samples of foreground galaxies that have been used for weak-lensing cross-correlation analysis in this paper.

2.2.1. Central galaxy samples

We use galaxies from the New York University Value Added Galaxy Catalog (NYU-VAGC[1], Blanton et al. 2005) of the Sloan

[1] http://sdss.physics.nyu.edu/vagc/

Digital Sky Survey Data Release 7 (SDSS DR7, Abazajian et al. 2009). Three selection criteria were applied to these galaxies: 1) r-band Petrosian apparent magnitude of $r \leq 17.72$; 2) spectroscopic redshift in the range of $0.01 \leq z \leq 0.2$; 3) redshift completeness of $C_z > 0.7$. We only use the central galaxies in our analysis. They are defined as the most massive galaxy in a galaxy group, which are identified by the group catalog (Yang et al. 2005, 2007)[2]. NYU-VAGC provides the measurements of stellar mass (M_*). We cross-matched our central galaxies with the MPA-JHU DR7 catalog[3], which provides galaxy star-formation rates (SFR, Brinchmann et al. 2004) derived from both spectroscopic and photometric data of SDSS.

In the overlapping sky area between SDSS and UNIONS, there are 126 675 central galaxies. We divided these galaxies into three stellar-mass bins: $9.0 \leq \log M_*/\mathrm{M}_\odot < 9.5$, $10.0 \leq \log M_*/\mathrm{M}_\odot < 10.5$, and $11.0 \leq \log M_*/\mathrm{M}_\odot < 11.5$. We further divided each stellar-mass bin into star-forming and quenched subsamples by using the demarcation line from Bluck et al. (2016).

2.2.2. Active galactic nuclei samples

The AGNs used here correspond to the type I sample described in Li et al. (2024). They are collected from two catalogs. The first one is the SDSS DR16 Quasar Catalog (Lyke et al. 2020). The total number of quasars is 750 414 with redshifts in the range of $0.1 < z < 6$. Their black-hole masses were estimated by Wu & Shen (2022) using the full width at half maximum of Hβ, Mg II, and C IV broad emission lines from spectroscopic observations. The black-hole masses used here correspond to the Hβ emission lines (see Wu & Shen 2022 for more details).

The second catalog is the SDSS DR7 AGN catalog (Liu et al. 2019), including both quasars and Seyfert galaxies. There are 14 584 AGNs with redshifts less than 0.35. Liu et al. (2019) used Hα and Hβ emission lines to measure their corresponding black-hole masses. We also adopted the black-hole mass based on the Hβ emission line.

We merged the two catalogs with duplicates removed, selecting AGNs in the redshift range of $0.05 < z < 0.6$. The final catalog of type I AGNs in the joint SDSS-UNIONS footprint contains 14, 649 objects. We divided these AGNs into low, medium, and high black-hole mass bins, which are $\log M_{\rm BH}/\mathrm{M}_\odot < 7.9$, $7.9 < \log M_{\rm BH}/\mathrm{M}_\odot < 8.5$, and $\log M_{\rm BH}/\mathrm{M}_\odot > 8.5$, respectively. It should be noted that the host galaxies of the selected AGNs include both central and satellite galaxies.

3. Methods of analysis

This section describes the methods of estimating the impact of PSF-induced systematics on galaxy ellipticity and tangential shear, $\gamma_{\rm t}$. We introduce the λ statistics as additive PSF systematics to the tangential shear. We discuss our measurement and modeling methodology and review how physical galaxy properties such as halo mass are derived from the measured tangential shear.

3.1. Point spread function error propagation

In general, the observed ellipticity, $\varepsilon^{\rm obs}$, of a galaxy is not an unbiased estimator of shear, γ, at that position. The relation between those quantities is, in complex notation to linear order,

$$\varepsilon^{\rm obs} = \varepsilon^{\rm s} + (1+m)\gamma + c + \delta\varepsilon + \alpha\varepsilon^{\rm psf}. \tag{1}$$

Here, $\varepsilon^{\rm s}$ denotes the intrinsic ellipticity of the galaxy, which is assumed to have a random orientation, and consequently has a vanishing expectation value, $\langle\varepsilon^{\rm s}\rangle = 0$. m and c are the multiplicative and additive biases, respectively. The fourth term on the right-hand side, $\delta\varepsilon$, represents the residual in the PSF at the galaxy position due to errors in PSF measurement, modeling, and interpolation. The final term quantifies the leakage from the PSF ellipticity into galaxy ellipticity, which can arise, for example, from an insufficient PSF correction during galaxy shape measurement. The coefficient, α, is the leakage amplitude.

These biases have a variety of origins (Massey et al. 2013): m can arise from the misestimation of the PSF (Gatti et al. 2021), but this effect is typically small (Massey et al. 2013). Larger contributions come from calibration errors in the shear measurement algorithm. The potential origins of c are PSF errors or the incomplete application of the charge transfer inefficiency (CTI) (van Uitert & Schneider 2016; Gatti et al. 2021).

In the model described by Eq. (1), we assume that m and c are not correlated with the PSF; we exclude PSF-induced effects from these two biases. The additive bias due to the PSF is shown in the last two terms in Eq. (1). We show below how the PSF uncertainty induces an additional multiplicative bias that is not included in the above equation. Since we are primarily focusing on PSF errors, we assume that the shear measurements have been accurately calibrated for m and c, and set $m = c = 0$.

Assuming ellipticity to be measured via second moments of the light distribution, the PSF residual has been derived via Gaussian error propagation in Paulin-Henriksson et al. (2008) as

$$\delta\varepsilon = \left(\varepsilon^{\rm obs} - \varepsilon^{\rm psf}\right)\frac{\delta T^{\rm psf}}{T} - \frac{T^{\rm psf}}{T}\delta\varepsilon^{\rm psf}, \tag{2}$$

where T is a measure of the galaxy's intrinsic (PSF deconvolved) size, and $T^{\rm psf}$ the PSF size. We note that these quantities scale with the area of the object; for a $2d$ Gaussian profile with scale σ, the relationship is $T = 2\sigma^2$. The PSF residual is induced by the error of the PSF model, which is denoted as the difference between the measured and modeled PSF in their size, $\delta T^{\rm psf}$, and ellipticity, $\delta\varepsilon^{\rm psf}$. Unfortunately, we cannot directly measure $\delta T^{\rm psf}$ and $\delta\varepsilon^{\rm psf}$ at galaxy positions. However, the PSF can be estimated using stars, and PSF residuals can be obtained at star positions. Therefore, we write Eq. (2) as

$$\delta\varepsilon = \left(\varepsilon^{\rm obs} - \varepsilon^{\rm psf}\right)\frac{T^{\rm psf}}{T}\frac{\delta T^{\rm psf}}{T^{\rm psf}} - \frac{T^{\rm psf}}{T}\delta\varepsilon^{\rm psf}, \tag{3}$$

and measure $T^{\rm psf}/T$ at galaxy positions, and $\delta T^{\rm psf}/T^{\rm psf}$ at star positions.

3.2. Point-spread-function-induced systematics for tangential shear

A sample, S, of objects that trace matter in the large-scale structure induces a tangential shear, $\gamma_{\rm t}^S$, on background galaxies. This tangential shear can be written as a second-order correlation between background shear and the foreground number density, n. Therefore, an average tangential shear caused by a foreground sample, S, is

$$\gamma_{\rm t}^S = \langle\gamma_{\rm t}\, n\rangle\,. \tag{4}$$

[2] https://gax.sjtu.edu.cn/data/Group.html
[3] https://wwwmpa.mpa-garching.mpg.de/SDSS/DR7/

The observed tangential shear can be expressed as

$$\hat{\gamma}_t \equiv \gamma_t^{obs} = \left\langle \varepsilon_t^{obs} n \right\rangle . \quad (5)$$

This calculation is the average of the observed tangential ellipticity of background galaxies, ε_t^{obs}, around foreground positions.

We can additionally define the cross-component of shear, $\gamma_\times$, rotated by 45 degrees with respect to γ_t. These two components can be combined to form the complex shear $\gamma = \gamma_t + i\gamma_\times$. The tangential shear, γ_t, is identified as E-mode, induced via gravitational lensing, whereas the cross-component, $\gamma_\times$, indicates the parity-odd B-mode.

We denote $\delta\gamma_t$ with

$$\delta\gamma_t = \gamma_t^{obs} - \gamma_t^S , \quad (6)$$

the difference between the observed and true shear. Inserting Eq. (1) into Eq. (5), we find the residual tangential shear component to be

$$\delta\gamma_t = \langle \varepsilon_t^s n \rangle + \left\langle \frac{T^{psf}}{T} \frac{\delta T^{psf}}{T^{psf}} \gamma_t n \right\rangle - \left\langle \frac{T^{psf}}{T} \frac{\delta T^{psf}}{T^{psf}} \varepsilon_t^{psf} n \right\rangle - \left\langle \frac{T^{psf}}{T} \delta\varepsilon_t^{psf} n \right\rangle + \left\langle \alpha \varepsilon_t^{psf} n \right\rangle . \quad (7)$$

The correlators can be further expanded under some assumptions, as follows. First, we can safely assume that the intrinsic galaxy ellipticity is uncorrelated with foreground number density. Next, we assume that the PSF model uncertainties are not correlated to the shear. Third, we separate out the prefactors T^{psf}/T and α, following Rowe (2010). This yields

$$\delta\gamma_t = \left\langle \frac{T^{psf}}{T} \right\rangle \left\langle \frac{\delta T^{psf}}{T^{psf}} \right\rangle \gamma_t^S - \left\langle \frac{T^{psf}}{T} \right\rangle \left\langle \frac{\delta T^{psf}}{T^{psf}} \varepsilon_t^{psf} n \right\rangle - \left\langle \frac{T^{psf}}{T} \right\rangle \left\langle \delta\varepsilon_t^{psf} n \right\rangle + \alpha \left\langle \varepsilon_t^{psf} n \right\rangle . \quad (8)$$

We define three new cross-correlation functions in analogy to the ρ statistics introduced for cosmic shear in Jarvis et al. (2016). These functions are

$$\lambda_1 = \left\langle \varepsilon_t^{psf} n \right\rangle ;$$
$$\lambda_2 = \left\langle \frac{\delta T^{psf}}{T^{psf}} \varepsilon_t^{psf} n \right\rangle ;$$
$$\lambda_3 = \left\langle \delta\varepsilon_t^{psf} n \right\rangle . \quad (9)$$

With that, we write the residual tangential shear as

$$\delta\gamma_t = \left\langle \frac{T^{psf}}{T} \right\rangle \left\langle \frac{\delta T^{psf}}{T^{psf}} \right\rangle \gamma_t^S + \alpha\lambda_1 - \left\langle \frac{T^{psf}}{T} \right\rangle (\lambda_2 + \lambda_3) . \quad (10)$$

The first term on the right-hand side, the prefactor of γ_t^S, is a PSF-induced multiplicative bias. The remaining three terms are PSF-induced additive biases, expressed as the λ statistics; that is, the correlations between the PSF and foreground positions. We used the TreeCorr[4] package (Jarvis 2015) to calculate the λ statistics. Their error bars were estimated using the jackknife method.

In the case of cosmic shear, the multiplicative term is usually ignored, and only the additive terms to the shear two-point correlation function, ξ_+, are kept. In the following, we consider both contributions using two different approaches. The first approach is indicated in Eq. (10), which assumes a knowledge of γ_t^S. However, γ_t^S is not a direct observable. Therefore, we adopted a theoretical model to derive γ_t^S given a sample of foreground tracers, S (see Sect. 3.3 for details). For the second approach, we calculated $\delta\gamma_t$ from the observation by combining Eqs. (6) and (10). Consequently, $\delta\gamma_t$ can be written as

$$\delta\gamma_t = \gamma_t^{obs} - \frac{\gamma_t^{obs} - \alpha\lambda_1 + \left\langle \frac{T^{psf}}{T} \right\rangle (\lambda_2 + \lambda_3)}{1 + \left\langle \frac{T^{psf}}{T} \right\rangle \left\langle \frac{\delta T^{psf}}{T^{psf}} \right\rangle} , \quad (11)$$

where γ_t^{obs} is measured by using the shear catalog around foreground tracers, S (see Section 3.4 for the calculation of γ_t^{obs}). In the limit where PSF-induced multiplicative bias vanishes, this expression reduces to Eq. (10).

We refer to the two expressions Eqs. (10) and (11) as the theory-based and observation-based approach, respectively. We denote the corresponding residual tangential shears as $\delta\gamma_t^{theory}$ and $\delta\gamma_t^{obs}$, respectively. We adopt the same $\left\langle \frac{T^{psf}}{T} \right\rangle$, $\left\langle \frac{\delta T^{psf}}{T^{psf}} \right\rangle$, and α in calculating $\delta\gamma_t^{theory}$ and $\delta\gamma_t^{obs}$. The values of these prefactors for UNIONS and DES catalogs are listed in Table 1, respectively.

Table 1. Prefactors and PSF leakage, α, for different catalogs.

Parameter	UNIONS	DES
$\left\langle \frac{T^{psf}}{T} \right\rangle$	1.3189	1.014
$\left\langle \frac{\delta T^{psf}}{T^{psf}} \right\rangle$	−0.0032	0.0003
$\left\langle \frac{T^{psf}}{T} \right\rangle \left\langle \frac{\delta T^{psf}}{T^{psf}} \right\rangle$	−0.0042	0.0003
α	0.033	0.001

3.3. Theory-based approach and its impact on constraining halo mass

The key ingredient of the theory-based approach (Eq. (10)) in calculating the residual tangential shear, $\delta\gamma_t^{theory}$, is the derivation of the model prediction, γ_t^S. We used an analytical method based on three assumptions. All galaxies from the foreground sample described in Sect. 2.2.1 are central galaxies. We have assumed that these galaxies follow the SHMR from Kravtsov et al. (2018). We calculated the average stellar mass of the galaxy sample and interpolated the SHMR to infer the average halo mass of the sample. We have also assumed that the halo is described by the Navarro–Frenk–White (Navarro et al. 1997, NFW) density profile and defined the halo mass as the total mass within a spherical region of radius r_{200m}, inside of which the mean mass density is equal to 200 times the mean matter density of the Universe. We further assumed that the halo mass and halo concentration satisfy the relation in Bhattacharya et al. (2013). With these assumptions, we can use the analytical equations from Yang et al. (2006) to derive the excess surface density, $\Delta\Sigma_t$.

The relation between $\Delta\Sigma_t$ and γ_t^S is given by the following equations:

$$\Delta\Sigma_t = \Sigma_{crit}\, \gamma_t^S ;$$
$$\Sigma_{crit}(z_l, z_s) = \frac{c^2}{4\pi G} \frac{D_s}{D_l D_{ls}} , \quad (12)$$

[4] https://pypi.org/project/TreeCorr/

where c is the speed of light, G is the gravitational constant, and D_l, D_s, and D_ls are the angular diameter distances to the lens, to the source, and between the lens and source, respectively. We adopted the mean redshift of the foreground galaxy sample to calculate z_l and the corresponding D_l. Instead of using a single source redshift value for z_s, we used the redshift distribution, $n(z)$, of the UNIONS catalog to derive Σ_crit via

$$\Sigma_\mathrm{crit}^{-1}(z_\mathrm{l}) = \int_{z_\mathrm{l}}^{z_\mathrm{lim}} \Sigma_\mathrm{crit}^{-1}(z_\mathrm{l}, z_\mathrm{s})\, n(z_\mathrm{s})\, \mathrm{d}z_\mathrm{s}, \tag{13}$$

where z_lim represents the maximum redshift value in the redshift distribution of the UNIONS catalog.

Taken together, we can derive γ_t^S, and hence $\delta\gamma_\mathrm{t}^\mathrm{theory}$. The above approaches were referred to as the Yang-halo model. The γ_t^S represents the true tangential shear that includes no systematics, while $\delta\gamma_\mathrm{t}^\mathrm{theory}$ corresponds to the PSF-induced systematical uncertainty in tangential shear. Thus, the combination of $\gamma_\mathrm{t}^S + \delta\gamma_\mathrm{t}^\mathrm{theory}$ corresponds to the inclusion of PSF-induced systematics to the true tangential shear, according to Eq. (6); that is, it corresponds to $\gamma_\mathrm{t}^\mathrm{obs}$. Therefore, we consider $\gamma_\mathrm{t}^S + \delta\gamma_\mathrm{t}^\mathrm{theory}$ to be an estimator of $\gamma_\mathrm{t}^\mathrm{obs}$ and denote it as $\hat{\gamma}_\mathrm{t}^\mathrm{obs}$.

To investigate the influence of the $\delta\gamma_\mathrm{t}^\mathrm{theory}$ on the estimated halo mass, we constrained the halo mass by fitting $\hat{\gamma}_\mathrm{t}^\mathrm{obs}$ using a modified version of the Yang-halo model: instead of using the halo mass – halo concentration relation from Bhattacharya et al. (2013), we set these two parameters as the free parameters in the model. The priors of these parameters were chosen to be flat, with the logarithm of the halo mass ($\log M_\mathrm{h}/\mathrm{M}_\odot$) in the range of [10.0, 16.0] and halo concentration in the range of [1.0, 16.0]. To constrain these parameters, we used *emcee*[5] (Foreman-Mackey et al. 2013) to run a Markov chain Monte Carlo (MCMC). The likelihood function was set to be

$$\ln \mathcal{L} = -\frac{1}{2}\left(\hat{\gamma}_\mathrm{t}^\mathrm{obs} - \gamma_\mathrm{t}^\mathrm{model}\right)^\mathrm{T} C^{-1} \left(\hat{\gamma}_\mathrm{t}^\mathrm{obs} - \gamma_\mathrm{t}^\mathrm{model}\right), \tag{14}$$

where $\gamma_\mathrm{t}^\mathrm{model}$ is the model prediction and C^{-1} is the inverse of the covariance matrix.

In the following, the constrained halo masses are the medium values of the posteriors, and the error bars correspond to 16 and 84% of the posterior distributions.

3.4. Observation-based approach and its impact on constraining halo mass

To apply the observation-based approach to study the PSF-induced systematics, we need to obtain the observed tangential shear, $\gamma_\mathrm{t}^\mathrm{obs}$, for a galaxy sample, as is shown in Eq. (11). We used the UNIONS shear catalog to calculate $\gamma_\mathrm{t}^\mathrm{obs}$. The ellipticities of galaxies in UNIONS are calibrated; therefore, the following equation is accurate enough to perform the calculation:

$$\gamma_\mathrm{t}^\mathrm{obs} = \frac{\sum_i^N w_i\, \varepsilon_{i,\mathrm{t}}}{\sum_i^N w_i}, \tag{15}$$

where w_i and $\varepsilon_{i,\mathrm{t}}$ are the weight and the ellipticity in the tangential direction around the lens of the source galaxy with index i, respectively. The sum was carried out over all suitable source galaxies. We calculated ε_t as

$$\varepsilon_\mathrm{t} = -\varepsilon_1 \cos 2\theta - \varepsilon_2 \sin 2\theta, \tag{16}$$

[5] https://emcee.readthedocs.io/en/stable/

where ε_1 and ε_2 are two ellipticity components of the source galaxy, and θ is the angle between the line connecting the lens and the source and the direction of increasing right ascension.

The source galaxies in UNIONS do not have photometric redshifts, and we used all of the sources in our calculations. Some source galaxies are thus in front of the "foreground" galaxies and will dilute the observed tangential shear. Eq. (13) models this dilution correctly.

Based on the UNIONS shear catalog and a given foreground galaxy sample, we applied TreeCorr to calculate its $\gamma_\mathrm{t}^\mathrm{obs}$. The error bars were estimated using the jackknife method.

We further quantified the impact of the observation-based approach on halo mass estimates. More specifically, we investigated the impact of PSF-induced systematics on the black-hole-mass – halo-mass relation. Li et al. (2024) recently investigated this relation for type I AGNs using the UNIONS shear catalog; we adopted the same method in Li et al. (2024) to calculate $\gamma_\mathrm{t}^\mathrm{obs}$, and therefore $\Delta\Sigma_\mathrm{t}$. Then, we derived $\delta\gamma_\mathrm{t}^\mathrm{obs}$ with Eq. (11). Following the method in Sect. 3.3, we treated $\gamma_\mathrm{t}^\mathrm{obs} - \delta\gamma_\mathrm{t}^\mathrm{obs}$ as an estimator of γ_t^S and denote it as $\hat{\gamma}_\mathrm{t}^S$, which represents the estimator of the true tangential shear without PSF-induced systematics.

We used the halo model introduced in Guzik & Seljak (2002) and applied in Li et al. (2024) to fit the excess surface density, $\Delta\Sigma_\mathrm{t}$, and $\Sigma_\mathrm{crit}\hat{\gamma}_\mathrm{t}^S$ of the AGN sample, respectively. Our model contains contributions from the central host halo, $\Delta\Sigma_\mathrm{cen}$, and satellite host halo, $\Delta\Sigma_\mathrm{sat}$. It further includes a baryonic term from the galaxy, $\Delta\Sigma_\mathrm{b}$, and a two-halo term from the neighbouring halos, $\Delta\Sigma_\mathrm{2h}$. The overall model is

$$\Delta\Sigma_\mathrm{t} = (1 - f_\mathrm{sat})\, \Delta\Sigma_\mathrm{cen} + f_\mathrm{sat}\, \Delta\Sigma_\mathrm{sat} + \Delta\Sigma_\mathrm{b} + \Delta\Sigma_\mathrm{2h}, \tag{17}$$

where f_sat describes the fraction of satellite galaxies in the sample.

We treated the baryonic contribution of the galaxy as a point mass and considered the stellar mass to be a free parameter in the model. The two-halo term was calculated by combining the halo bias model from Tinker et al. (2010) and the linear matter-matter correlation function from COLOSSUS (Diemer 2018). The model contains a total of three free parameters, which are the halo mass (M_h), the stellar mass (M_*), and the satellite fraction (f_sat), respectively. We constrained these parameters by running MCMC with the *emcee* package. The likelihood function is the same as Eq. (14). We refer to the above model as the AGN-halo model (see Li et al. 2024 for more details on calculating and modeling the weak-lensing signals of the AGN samples).

We discussed several versions of tangential shear above, and to make it easier for the reader to distinguish between them, we have listed their definitions in Table 2.

3.5. Halo mass change and tangential shear residuals

The average halo mass of a galaxy sample derived from $\hat{\gamma}_\mathrm{t}^\mathrm{obs}$ in the manner described in Sect. 3.3 might be biased by PSF-induced systematics. To visualize this potential change in halo mass, we defined a halo mass, M_h^P, modified by a percentage, P, as

$$M_\mathrm{h}^P = M_\mathrm{h} \cdot (1 + P). \tag{18}$$

where M_h corresponds to the halo mass derived from the SHMR. In this way, we can evaluate the percentage change in halo mass corresponding to PSF-induced residual tangential shear, $\delta\gamma_\mathrm{t}(\theta)$, at different angular scales, θ. As before, we used the Yang-halo model to generate the tangential shears corresponding to different M_h^P.

Table 2. Definition of different tangential shears.

Tangential shears	Definitions
γ_t^S	The true tangential shear
γ_t^{obs}	The observed tangential shear
$\delta\gamma_t^{theory}$	PSF-induced residual tangential shear calculated by the theory-based approach (Eq. (10))
$\delta\gamma_t^{obs}$	PSF-induced residual tangential shear calculated by the observation-based approach (Eq. (11))
$\hat{\gamma}_t^S$	The estimator of the true tangential shear calculated by γ_t^{obs}-$\delta\gamma_t^{obs}$
$\hat{\gamma}_t^{obs}$	The estimator of the observed tangential shear calculated by γ_t^S+$\delta\gamma_t^{theory}$

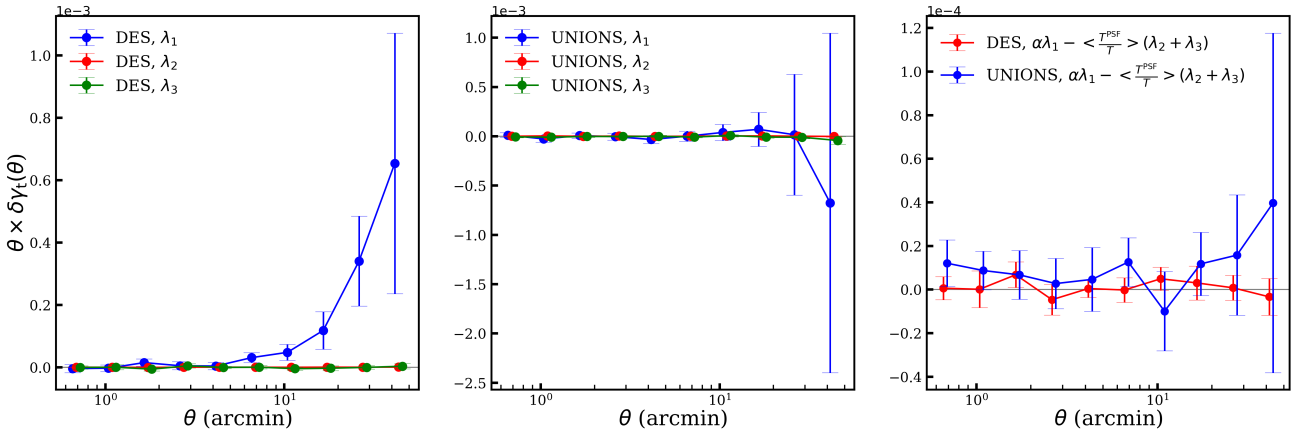

Fig. 1. Comparison of the PSF-induced bias for the DES and UNIONS catalogs based on random positions. The left and middle panels show the three λ statistics for the DES and UNIONS catalogs, respectively. The right panel shows the PSF-induced additive bias for the DES and UNIONS in red and blue, respectively. The error bars correspond to the 1σ uncertainty using the jackknife method.

4. Results

In this section, we present our results on the impact of PSF-induced multiplicative and additive biases on galaxy-galaxy lensing.

4.1. Point-spread-function-induced multiplicative bias

As was introduced in Eq. (10), the multiplicative bias associated with the PSF manifests itself as a prefactor. Table 1 shows the average prefactors for both the UNIONS and DES catalogs. The PSF leakage, α, is typically computed via ratios of galaxy- and PSF auto- and cross-correlations. We quote its values from Guinot et al. (2022) and Gatti et al. (2021) for the UNIONS and DES catalogs, respectively. For α in the UNIONS catalog, Guinot et al. (2022) fit values of α at different angular scales. The average value for all scales in the model fitting method is $\alpha = 0.033$.

The PSF-induced multiplicative biases in both catalogs are lower than 1%, indicating that their PSFs are well calibrated. This bias is thus smaller than the typical residual multiplicative bias of current weak-lensing surveys, which is on the order of 1–2% (e.g., Giblin et al. 2021; MacCrann et al. 2022). We conclude that the PSF uncertainty is not a major contributor to the multiplicative bias.

4.2. Point-spread-function-induced additive bias

To examine the overall intrinsic bias levels of the DES and UNIONS catalogs, we randomly generated 2 000 000 positions in the survey footprints. We used these random samples as the position catalog, n, in Eq. (9). This gives us an indication of a correlation between the PSF and the footprint mask. The λ statistics for the DES and UNIONS catalogs based on random positions are shown in the left and middle panels of Fig. 1, respectively. We find that the λ_2 and λ_3 in the DES and UNIONS catalogs are broadly consistent with zero, but the λ_1 in both catalogs deviates from zero at large angular scales and with large errors.

We also show the residual tangential shear (additive terms of Eq. (10)) in the right panel of Fig. 1. The PSF-induced additive biases for UNIONS and DES are broadly consistent with zero within the margin of error. The results from the DES catalog show a lower level of systematics compared to the results from the UNIONS catalog. The consistency with zero on most angular scales indicates an accurate PSF correction for both surveys. However, in regimes in which the tangential shear induced by a density tracer is below a few $\times 10^{-6}$, the gravitational lensing shear might be significantly affected by PSF errors.

Previous weak-lensing-based studies have investigated the relation between galaxy stellar mass and halo mass and found a positive correlation between these two quantities. The dispersion in this relation is however large. In addition, at fixed stellar mass, quenched galaxies tend to reside in more massive halos compared to star-forming galaxies (Mandelbaum et al. 2016; Bilicki et al. 2021; Zhang et al. 2021, 2024). Here, we investigate whether PSF-induced systematics can bias the relation between galaxy properties and halo mass.

Galaxy samples have selection functions that depend on their properties; for example, size, magnitude, or star-formation rate. The galaxy selection can vary with observing conditions such as seeing, image quality, and local star and galaxy density. Since

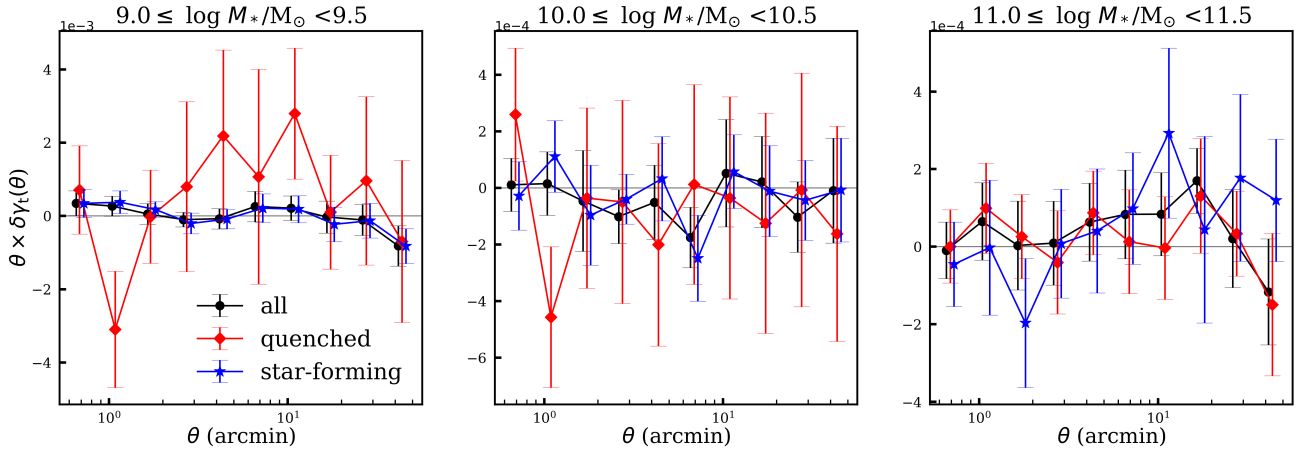

Fig. 2. PSF-induced additive bias for the central galaxy samples with different stellar mass and SFR. The three panels correspond to the three stellar-mass bins. In each panel, black circles show all galaxies in the stellar-mass bin, while the red diamonds (blue stars) correspond to the quenched (star-forming) subsample. These calculations are based on the UNIONS catalog.

these factors also depend on the PSF, the galaxy-galaxy lensing PSF systematics discussed in this work can vary between different foreground samples.

We calculated the dependence of PSF-induced additive bias on the foreground galaxy samples with different stellar masses as well as SFRs (see Sect. 2.2.1 for the sample selections). We focused on the UNIONS catalog and its large overlap with SDSS/eBOSS. The PSF-induced additive biases based on different stellar-mass samples are shown in Fig. 2. In each stellar-mass bin, PSF-induced bias is consistent with zero on most angular scales. This indicates that PSF-induced systematics do not have a significant effect on the galaxy-galaxy lensing of these samples.

Also shown are PSF-induced additive biases for subsamples with different SFRs. Overall, the biases of the quenched and star-forming subsamples are consistent within the error bars. Therefore, we do not find a significant dependence of PSF-induced additive bias on stellar mass and SFR.

4.3. The overall point-spread-function-induced systematics on weak-lensing measurements

We now turn to the overall effect of PSF-induced biases on weak-lensing measurements and halo mass estimates. We used stellar-mass samples described in Section 4.2 as density tracers and the UNIONS star and galaxy catalogs as shape catalogs.

We first applied the theory-based approach introduced in Sect. 3.3 to predict the theoretical tangential shear, γ_t^S, of the foreground galaxy sample. With that, we calculated the residual tangential shear, $\delta\gamma_t^{\rm theory}$, using Eq. (10). Following the method in Sect. 3.3 (see also Table 2), we adopted $\hat{\gamma}_t^{\rm obs} \equiv \gamma_t^S + \delta\gamma_t^{\rm theory}$ as the estimator of the observed tangential shear that now includes PSF-induced systematics. We then fitted the model described in Sect. 3.3 to $hat\gamma_t^{\rm obs}$. By comparing the model fit halo mass with the corresponding halo mass of γ_t^S, we can quantify the difference in halo mass due to PSF-induced systematics. The results are shown in the upper panels of Fig. 3.

The tangential shear is most affected by the PSF in the lowest stellar mass bin, and mainly on small angular scales. The corresponding halo mass is biased by up to 18%. For higher stellar masses, the measured halo masses deviate by 11 and 1%, respectively.

Next, we applied the observation-based approach. We calculated the observed tangential shear, $\gamma_t^{\rm obs}$, for the above galaxy samples, computed $\delta\gamma_t^{\rm obs}$ using Eq. (11), and adopted $\hat{\gamma}_t^S \equiv \gamma_t^{\rm obs} - \delta\gamma_t^{\rm obs}$ as the estimator of the true tangential shear, γ_t^S. The comparisons are shown in the lower panels of Fig. 3. Similar to the theory-based approach, PSF-induced systematics mainly affect the results in the low stellar mass range at a level that is smaller than the statistical errors.

We compared PSF-induced systematics from the two approaches and also the residual tangential shear due to halo mass change (for calculating the halo mass-induced residual tangential shear, see Sect. 3.5) in Fig. 4. The theory- and observation-based approaches yield similar results. As is discussed in Sect. 4.2, the PSF-induced multiplicative bias is very small so that the residual tangential shear, $\delta\gamma_t$, is dominated by the λ statistics (PSF-induced additive bias). We further compared the halo mass-induced residual tangential shear with the PSF-induced residual tangential shear. On individual angular scales, PSF-induced systematics can impact the tangential shear corresponding to a change in halo mass significantly exceeding the average bias of the halo mass. Such residuals can be removed using the methods described in this work.

Our analysis suggests that the weak-lensing measurements for the low-mass galaxies are facing potential challenges from PSF-induced systematics. In addition, the galaxy number density of these galaxies is low. The current survey depths are insufficient to detect more low-mass central galaxies. Together, these drawbacks make the accuracy of the weak-lensing measurements at the low-mass end always low. The error bars in the lensing signals are more significant than the PSF-induced systematics we detect here, making PSF-induced systematics less important. However, our work may inspire future studies using deeper data, for which correcting for PSF-induced systematics may become important.

4.4. Impact of point-spread-function-induced systematics on the black-hole-mass – halo-mass relation

Recently, Li et al. (2024) studied the black-hole-mass – halo-mass relation based on SDSS AGNs as foreground samples and UNIONS as the background shear catalog. We now quantify the impact of PSF-induced systematics on the halo mass estimates for the type I AGN samples.

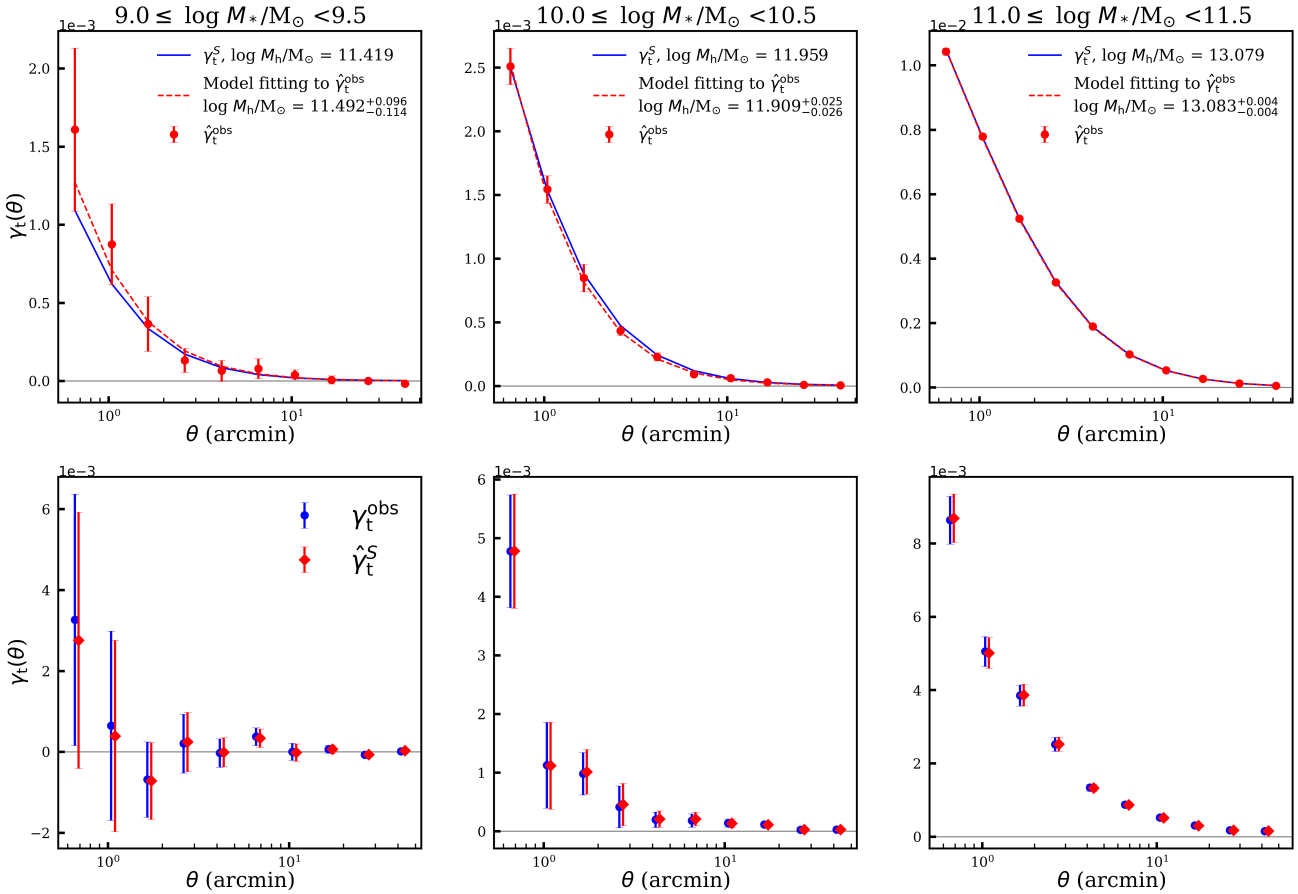

Fig. 3. Effect of PSF-induced systematics in UNIONS weak lensing by the theory-based and observation-based approaches. Different columns correspond to the results of galaxy samples in different stellar mass bins. In each upper panel, the solid blue line is the theoretical γ_t^S, while the red circles with error bars and the dashed red line are the estimator of the observed tangential shear ($\hat{\gamma}_t^{obs}$) and model fitting, respectively. Their corresponding halo masses are also labeled in the panel. In each lower panel, the blue and red symbols with error bars correspond to the observed tangential shear (γ_t^{obs}) calculated from the UNIONS shear catalog and the estimator of the true tangential shear ($\hat{\gamma}_t^S$), respectively.

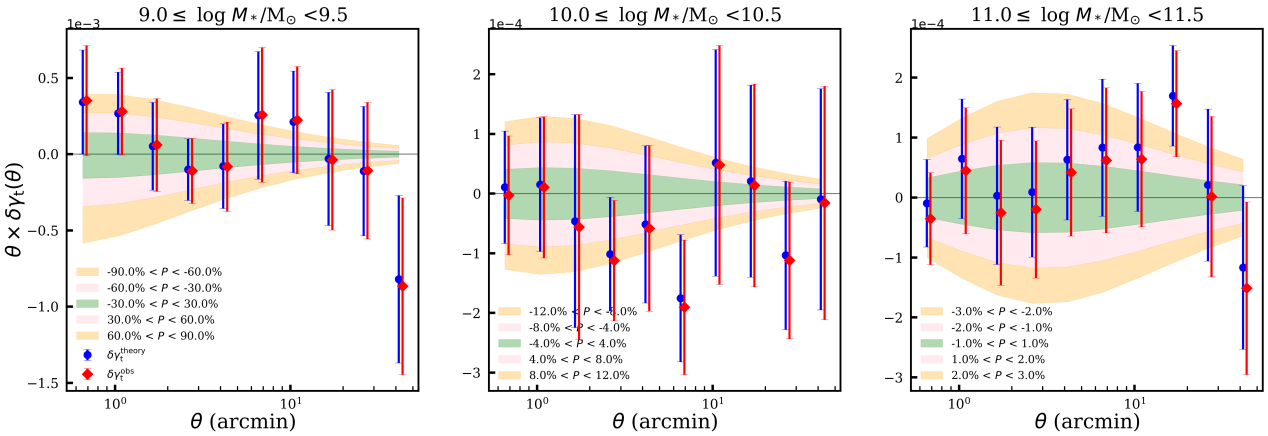

Fig. 4. Comparison of $\delta\gamma_t^{theory}$ and $\delta\gamma_t^{obs}$ and the halo mass-induced residual tangential shears from UNIONS. Different panels correspond to the results in different stellar mass bins. In each panel, the blue and red symbols with error bars correspond to the $\delta\gamma_t$ from the theory-based and observation-based approaches, respectively. Shaded regions of different colors correspond to the different degrees of the halo mass-induced shear residuals.

We began by constructing the foreground samples as in Li et al. (2024) (see Section 2.2.2 for the sample selections). We then used the methods in Sect. 3.4 to calculate γ_t^{obs}, $\hat{\gamma}_t^S$ (see also Table 2) and their corresponding model fit results, respectively. These results are shown in Fig. 5.

The weak-lensing tangential shears in the three black-hole mass bins are weakly affected by PSF-induced systematics on scales larger than 2 arcmin. The largest differences appear in the low-black-hole-mass sample. We used the AGN-halo model (see Section 3.4) to measure the halo masses for the three AGN

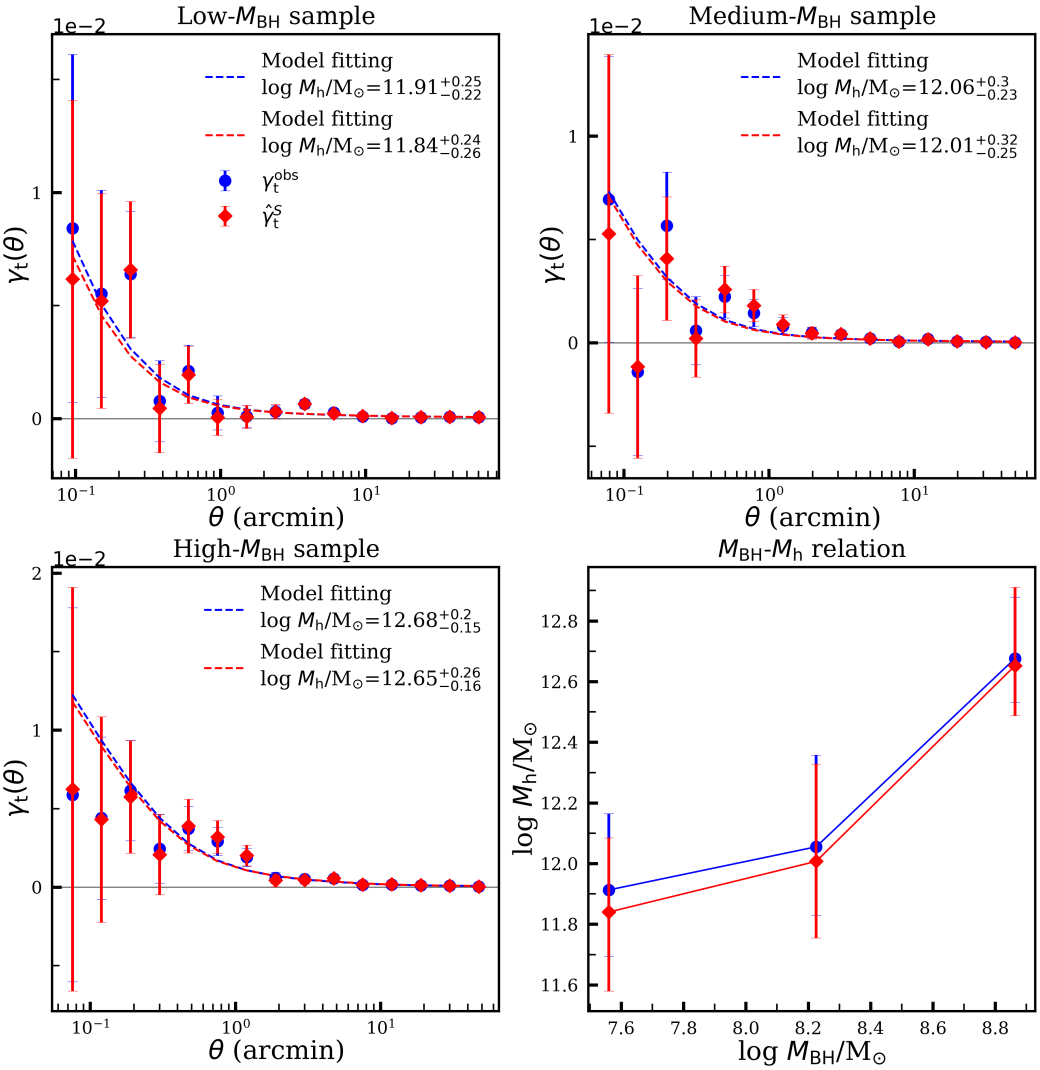

Fig. 5. Effect of PSF-induced systematics on the black-hole-mass – halo-mass relation, measured with UNIONS. The upper left, upper right, and lower left panels correspond to the low, medium, and high-black-hole mass AGN samples, respectively. In each panel, blue (red) symbols show the raw measured $\gamma_{\rm t}^{\rm obs}$ (PSF-induced systematics corrected $\hat{\gamma}_{\rm t}^{S}$) tangential shear; lines correspond to the results of the model fitting, with the corresponding fit halo mass indicated in the panel (see Section 3.4). The lower right panel shows the black-hole-mass – halo-mass relation using the raw measured (PSF-induced systematics corrected) halo masses in blue (red).

samples. Their black-hole-mass – halo-mass relations are shown in the lower-right panel of Figure 5. Ignoring PSF-induced biases leads to a slight but systematic underestimation of the halo masses in the low and medium-black-hole mass samples, with the degree of deviation of their halo masses being 15 and 11%, respectively. These halo mass deviations are however smaller than the statistical errors.

5. Discussion

5.1. Motivation for the λ statistics

In analyses of weak-lensing correlations with density tracers – for example, weak lensing of clusters or galaxy-galaxy lensing – null tests and diagnostics of additive biases are used routinely. These are, for example, the mean tangential shear around non-tracers such as random points, stars, or coordinates relative to the CCDs, and the cross-component of shear around tracers or non-tracer points Mandelbaum et al. (2005). These correlations are either found to be consistent with zero or very small and then discarded, or they are subtracted from the tangential shear to remove this potential systematic effect from the data.

The λ statistics Eq. (10) introduced here are motivated in a similar way. They extend those previous works by quantifying the contribution of PSF-induced systematics for lensing by foreground density tracers. In particular, our formalism allows for the propagation of PSF errors to derived physical quantities. Such quantities are, for example, the average halo mass of foreground galaxy samples, as is illustrated in this paper. Other examples not studied here are the halo concentration, galaxy bias parameters, cluster mass calibration for cosmology, the intrinsic galaxy alignment amplitude, and void density profiles, to name just a few.

We argue that residuals quantified by the λ statistics are present in all weak-lensing measurements of density tracers. This is due to the spatially varying PSF within the FoV, a phenomenon that can lead to a correlation between the PSF and sky position.

Some of the PSF residuals can in principle be removed from the tangential shear from a density tracer by subtracting the shear around random points. However, this does not remove

correlations between PSF and tracer number density. This was noted in Mandelbaum et al. (2005). The λ statistics quantify this correlation, and correspond to the term $\langle \delta n\, \gamma_{\rm sys} \rangle$ in Eq. (26) of Mandelbaum et al. (2005).

5.2. Interpretation of the λ-statistic terms

We now provide an intuitive interpretation of the three λ-statistic terms. The function, λ_1, is qualitatively different from the other two, λ_2 and λ_3, which can be grouped together.

The first function, λ_1, quantifies the correlation between tangential PSF ellipticity and foreground sample position. The function, λ_1, is proportional to the PSF ellipticity, not its residual, and can be on the order of 10%. For example, the requirement on the PSF ellipticity for the Euclid space mission is 0.15 (Laureijs et al. 2011); in UNIONS, the focal-plane PSF ellipticity averaged over atmospheric fluctuations is on the order of 0.05 (Guinot et al. 2022). Multiplied with a PSF leakage, α, at the percent level (Giblin et al. 2021; Gatti et al. 2021, e.g.,) yields an additive PSF-induced bias, naïvely on the order of 10^{-4}–10^{-3}, which is indeed in the range of sought-after weak-lensing shear correlations.

For the λ_1-term to impact the measured tangential shear, the PSF ellipticity needs to display a spatial pattern that is correlated to the positions of the foreground sample. An example is the commonly observed circular PSF pattern in the focal plane and the foreground sample being a cluster (sample) near the image centre. We note that the λ_1 term is independent of the quality of the PSF model.

The second function, λ_2, weighs the PSF ellipticity-foreground position correlation by the relative PSF size residual. This function shows some similarity to $\rho_5 = \langle \varepsilon^{\rm psf} (\varepsilon^{\rm psf,*} \delta T^{\rm psf}/T^{\rm psf}) \rangle$ for cosmic shear (see Appendix A). The third function, λ_3, is the correlation of PSF ellipticity residuals with foreground positions, having a resemblance in $\rho_2 = \langle \varepsilon^{\rm psf} \delta\varepsilon^{\rm psf,*} \rangle$. Both the second and third λ statistics contribute to galaxy-galaxy lensing in the presence of PSF residuals that are spatially correlated to the positions of the foreground sample. Such correlations can be induced where detection and selection of the density tracer populations depend on the PSF. Examples where PSF residuals can affect the tracer number density are:

- seeing and depth variations;
- star-galaxy separation, and cross-contamination of both samples;
- detector effects such as CTI
- survey strategy; for example scan direction, or fiber placement;
- photometry and photometric redshifts;
- local object density (crowded fields) and extinction.

In all of these cases, spurious correlations between PSF residuals and tracer positions might be introduced that will be captured by λ_2 and λ_3. Some of those effects such as varying seeing will only give rise to PSF – number density correlations if the lensing and density tracer catalogs originate from the same data. Others, such as crowded fields, are intrinsic. The contamination of the PSF sample by density tracer objects and vice versa can induce systematic biases studied here, even if they are selected from different surveys, if the target sample consists of small objects close in size to the PSF in either survey.

5.3. Comparison to the ρ statistics for cosmic shear

Contrary to the ρ statistics that were introduced to quantify PSF systematics for cosmic shear, the λ statistics do not involve correlations between PSF uncertainties. Instead, they quantify the correlation of PSF residuals with respect to foreground positions.

The conditions for nonvanishing λ statistics are stronger than for $\rho \neq 0$. In both cases, we need an imperfect PSF model or PSF leakage that displays a spatial pattern. In addition, for the λ statistics to be significant, the PSF residual pattern also needs to be correlated to the positions of the density tracer in question.

Related to this is the second difference between λ and ρ: Cosmic shear involves second-order correlations of the statistical homogeneous and isotropic galaxy shear field. The ρ statistics are evaluated not at galaxy positions but at star positions. The star or PSF ellipticity field can be assumed to be statistically homogeneous and isotropic. This allows for the addition of the measured ρ and ξ_+.

Galaxy-galaxy lensing, however, is the cross-correlation between two correlated fields, background shear and foreground density. The second-order correlation estimators are not invariant under translation or rotation of only one of the fields. To capture PSF systematic correlations, we need to use the actual galaxy positions.

6. Summary

This paper introduces PSF-induced systematics for weak-lensing cross-correlations with foreground density tracers. We have developed a theoretical framework for quantifying PSF-induced systematics that contributes to both the multiplicative and the additive bias in weak-lensing tangential shear. In particular, we introduce three scale-dependent ellipticity-position correlation functions dubbed "λ statistics" to characterize PSF-induced additive biases. These correlation functions can be computed from the information about ellipticities and size residuals of the PSF, and the positions of the foreground sample. In this framework, PSF-induced systematics propagate to physical parameters of the density tracer sample measured from weak lensing.

The PSF-induced multiplicative bias is a prefactor in the residual tangential shear. We used the UNIONS and DES weak-lensing catalogs to calculate PSF-induced multiplicative bias, which we find to be −0.0042 and 0.0003, respectively. This is a subdominant contribution to the overall multiplicative bias of current weak-lensing surveys.

We quantified the impact of PSF-induced systematics on the halo masses of two cases of the foreground galaxy samples. The first case is a sample of central galaxies from the Yang group catalog (Yang et al. 2005, 2007), which we split into subsamples by stellar mass and star-formation rate. The PSF-induced bias acts mainly on small angular scales and low stellar masses. The largest resulting bias in the weak-lensing derived halo mass is 18% for the subsample in the stellar mass range of $9 \leq \log M_*/{\rm M}_\odot < 9.5$.

The second case is the type I AGN sample, used in Li et al. (2024) to estimate the black-hole-mass – halo-mass relation. We calculated the impact of PSF-induced systematics on the halo mass estimation. Similar to the previous case, PSF-induced systematics is most important on small angular scales and absent on large angular scales. Without accounting for PSF-induced systematics, the halo mass is underestimated at low black-hole masses.

Our proposed framework can be used for quality-checking of weak-lensing – density cross-correlations. It is straightforward to extend the formalism to weak-lensing-like observables and estimators such as intrinsic alignments of galaxies.

Acknowledgements. We thank the anonymous referee for providing their report with useful feedback that helped us to improve the draft. This work was made possible by utilizing the CANDIDE cluster at the Institut d'Astrophysique de Paris, which was funded through grants from the PNCG, CNES, DIM-ACAV, and the Cosmic Dawn Center and maintained by S. Rouberol. We are honored and grateful for the opportunity of observing the Universe from Maunakea and Haleakala, which both have cultural, historical and natural significance in Hawai'i. This work is based on data obtained as part of the Canada-France Imaging Survey, a CFHT large program of the National Research Council of Canada and the French Centre National de la Recherche Scientifique. Based on observations obtained with MegaPrime/MegaCam, a joint project of CFHT and CEA Saclay, at the Canada-France-Hawaii Telescope (CFHT) which is operated by the National Research Council (NRC) of Canada, the Institut National des Science de l'Univers (INSU) of the Centre National de la Recherche Scientifique (CNRS) of France, and the University of Hawaii. This research used the facilities of the Canadian Astronomy Data Centre operated by the National Research Council of Canada with the support of the Canadian Space Agency. This research is based in part on data collected at Subaru Telescope, which is operated by the National Astronomical Observatory of Japan. Pan-STARRS is a project of the Institute for Astronomy of the University of Hawai'i, and is supported by the NASA SSO Near Earth Observation Program under grants 80NSSC18K0971, NNX14AM74G, NNX12AR65G, NNX13AQ47G, NNX08AR22G, 80NSSC21K1572 and by the State of Hawai'i. This work was supported in part by the Canadian Advanced Network for Astronomical Research (CANFAR) and Compute Canada facilities. This work was funded by the China Scholarship Council (CSC).

References

Abazajian, K. N., Adelman-McCarthy, J. K., Agüeros, M. A., et al. 2009, ApJS, 182, 543
Bhattacharya, S., Habib, S., Heitmann, K., & Vikhlinin, A. 2013, ApJ, 766, 32
Bilicki, M., Dvornik, A., Hoekstra, H., et al. 2021, A&A, 653, A82
Blanton, M. R., Schlegel, D. J., Strauss, M. A., et al. 2005, AJ, 129, 2562
Bluck, A. F. L., Mendel, J. T., Ellison, S. L., et al. 2016, MNRAS, 462, 2559
Bower, R. G., Schaye, J., Frenk, C. S., et al. 2017, MNRAS, 465, 32
Brinchmann, J., Charlot, S., White, S. D. M., et al. 2004, MNRAS, 351, 1151
Diemer, B. 2018, ApJS, 239, 35
Euclid Collaboration (Scaramella, R., et al.) 2022, A&A, 662, A112
Farrens, S., Guinot, A., Kilbinger, M., et al. 2022, A&A, 664, A141
Foreman-Mackey, D., Hogg, D. W., Lang, D., & Goodman, J. 2013, PASP, 125, 306
Gatti, M., Sheldon, E., Amon, A., et al. 2021, MNRAS, 504, 4312
Giblin, B., Heymans, C., Asgari, M., et al. 2021, A&A, 645, A105
Guinot, A., Kilbinger, M., Farrens, S., et al. 2022, A&A, 666, A162
Guzik, J., & Seljak, U. 2002, MNRAS, 335, 311
Jarvis, M. 2015, Astrophysics Source Code Library [record ascl:1508.007]
Jarvis, M., Sheldon, E., Zuntz, J., et al. 2016, MNRAS, 460, 2245
Jarvis, M., Bernstein, G. M., Amon, A., et al. 2021, MNRAS, 501, 1282
Kilbinger, M. 2015, Rep. Prog. Phys., 78, 086901
Kravtsov, A. V., Vikhlinin, A. A., & Meshcheryakov, A. V. 2018, Astron. Lett., 44, 8
Laureijs, R., Amiaux, J., Arduini, S., et al. 2011, arXiv e-prints [arXiv:1110.3193]
Leauthaud, A., Tinker, J., Bundy, K., et al. 2012, ApJ, 744, 159
Li, Q., Kilbinger, M., Luo, W., et al. 2024, ApJL, submitted [arXiv:2402.10740]
Liaudat, T., Bonnin, J., Starck, J.-L., et al. 2021, A&A, 646, A27
Liaudat, T. I., Starck, J.-L., & Kilbinger, M. 2023, Front. Astron. Space Sci., 10, 1158213
Liu, H.-Y., Liu, W.-J., Dong, X.-B., et al. 2019, ApJS, 243, 21
Luo, W., Yang, X., Lu, T., et al. 2018, ApJ, 862, 4
Lyke, B. W., Higley, A. N., McLane, J. N., et al. 2020, ApJS, 250, 8
MacCrann, N., Becker, M. R., McCullough, J., et al. 2022, MNRAS, 509, 3371
Mandelbaum, R. 2018, ARA&A, 56, 393
Mandelbaum, R., Hirata, C. M., Seljak, U., et al. 2005, MNRAS, 361, 1287
Mandelbaum, R., Seljak, U., Kauffmann, G., Hirata, C. M., & Brinkmann, J. 2006, MNRAS, 368, 715
Mandelbaum, R., Wang, W., Zu, Y., et al. 2016, MNRAS, 457, 3200
Massey, R., Hoekstra, H., Kitching, T., et al. 2013, MNRAS, 429, 661
Moster, B. P., Somerville, R. S., Maulbetsch, C., et al. 2010, ApJ, 710, 903
Navarro, J. F., Frenk, C. S., & White, S. D. M. 1997, ApJ, 490, 493
Paulin-Henriksson, S., Amara, A., Voigt, L., Refregier, A., & Bridle, S. L. 2008, A&A, 484, 67
Planck Collaboration XIII. 2016, A&A, 594, A13
Posti, L., Fraternali, F., & Marasco, A. 2019, A&A, 626, A56
Rowe, B. 2010, MNRAS, 404, 350
Shankar, F., Allevato, V., Bernardi, M., et al. 2020, Nat. Astron., 4, 282
Tinker, J. L., Robertson, B. E., Kravtsov, A. V., et al. 2010, ApJ, 724, 878
van Uitert, E., & Schneider, P. 2016, A&A, 595, A93
Velander, M., van Uitert, E., Hoekstra, H., et al. 2014, MNRAS, 437, 2111
Viola, M., Cacciato, M., Brouwer, M., et al. 2015, MNRAS, 452, 3529
Wu, Q., & Shen, Y. 2022, ApJS, 263, 42
Yang, X., Mo, H. J., van den Bosch, F. C., & Jing, Y. P. 2005, MNRAS, 356, 1293
Yang, X., Mo, H. J., van den Bosch, F. C., et al. 2006, MNRAS, 373, 1159
Yang, X., Mo, H. J., van den Bosch, F. C., et al. 2007, ApJ, 671, 153
Yang, X., Mo, H. J., & van den Bosch, F. C. 2009, ApJ, 695, 900
Zhang, Z., Wang, H., Luo, W., et al. 2021, A&A, 650, A155
Zhang, Z., Wang, H., Luo, W., et al. 2022, A&A, 663, A85
Zhang, Z., Wang, H., Luo, W., et al. 2024, ApJ, 960, 71

Appendix A: ρ statistics for cosmic shear

Two correlation functions between PSF ellipticity and its residuals were introduced in Rowe (2010). The purpose of those diagnostics was to distinguish between different PSF models in a quantitative way In particular, the second correlation function, D_2, corresponding to ρ_2 in the Jarvis et al. (2016) notation, is an indication of over-fitting. In that case the PSF model fits part of the noise, which creates a correlation between the observed PSF ellipticity and the model (residual).

These correlations were generalised in Jarvis et al. (2016). This work rederived the two original Rowe (2010) diagnostics and three additional functions by considering the two-point correlator of Eq. (1), which is an estimator of the shear two-point correlation function,

$$\hat{\xi}_+(\theta) = \left\langle \varepsilon^{\rm obs} \varepsilon^{\rm obs,*} \right\rangle(\theta), \tag{A.1}$$

into which Eq. (3) is inserted. The ρ statistics are defined as second-order correlation functions

$$\begin{aligned}
\rho_1(\theta) &= \left\langle \delta\varepsilon^{\rm psf}\, \delta\varepsilon^{\rm psf,*} \right\rangle(\theta);\\
\rho_2(\theta) &= \left\langle \varepsilon^{\rm psf}\, \delta\varepsilon^{\rm psf,*} \right\rangle(\theta);\\
\rho_3(\theta) &= \left\langle \left(\varepsilon^{\rm psf} \frac{\delta T^{\rm psf}}{T^{\rm psf}}\right)\left(\varepsilon^{\rm psf,*} \frac{\delta T^{\rm psf}}{T^{\rm psf}}\right) \right\rangle(\theta);\\
\rho_4(\theta) &= \left\langle \delta\varepsilon^{\rm psf} \left(\varepsilon^{\rm psf,*} \frac{\delta T^{\rm psf}}{T^{\rm psf}}\right) \right\rangle(\theta);\\
\rho_5(\theta) &= \left\langle \varepsilon^{\rm psf} \left(\varepsilon^{\rm psf,*} \frac{\delta T^{\rm psf}}{T^{\rm psf}}\right) \right\rangle(\theta).
\end{aligned} \tag{A.2}$$

With some prefactors that depend on the ratio between PSF and galaxy size and the leakage parameter α, the five ρ-statistic functions are written as additive terms to the cosmological shear two-point correlation function ξ_+, estimated by the correlation of observed galaxy ellipticities.

The choice to leave the size ratio and leakage parameters out of the ρ statistics is conveniently done such that the quantities to correlate only depend on quantities that are available at star positions. In Rowe (2010) the size ratio and leakage parameter are computed independently from the ρ statistics.

The ensemble average of the ρ statistics is thus estimated using star position, whereas the two-point correlation function ξ_+ is estimated by averaging over galaxy positions. Both can be added if both stars and galaxies randomly sample the underlying PSF and cosmic-shear fields, respectively.

The case of galaxy-galaxy lensing is more complex since the λ statistics involve star - galaxy cross-correlations.